# Interaction of complex fluids and solids: Theory, algorithms and application to phase-change-driven implosion

**Jesus Bueno** · **Carles Bona-Casas** · **Yuri Bazilevs** · **Hector Gomez**

**Abstract** There is a large body of literature dealing with the interaction of solids and classical fluids, but the mechanical coupling of solids and complex fluids remains practically unexplored, at least from the computational point of view. Yet, complex fluids produce much richer physics than classical fluids when they interact with solids, especially at small scales. Here, we couple a nonlinear hyperelastic solid with a single-component two-phase flow where the fluid can condensate and evaporate naturally due to temperature and/or pressure changes. We propose a fully-coupled fluid–structure interaction algorithm to solve the problem. We illustrate the viability of the theoretical framework and the effectiveness of our algorithms by solving several problems of phase-change-driven implosion, a physical process in which a thin structure collapses due to the condensation of a fluid.

J. Bueno (✉)
University of A Coruña
Campus de Elviña, 15192, A Coruña, Spain
Tel.: +34-981-167000 Ext.: 5470
E-mail: jesus.bueno@udc.es

H. Gomez - C. Bona-Casas
Department of Mathematical Methods,
University of A Coruña
Campus de Elviña, 15192, A Coruña, Spain

Y. Bazilevs
Department of Structural Engineering,
University of California, San Diego
9500 Gilman Drive, La Jolla, CA 92093, USA

## 1 Introduction

### 1.1 Interaction of complex fluids and solids

Traditional fluid–structure interaction (FSI) methods have mainly focused on the interaction of solids with classical fluids governed by the Navier–Stokes equations of incompressible or compressible flows [8, 26, 45–47, 55, 58, 60, 63, 64, 67, 70, 72, 66]. Yet, there are a number of open FSI problems that cannot be modeled using this paradigm because they fundamentally depend on physical mechanisms not captured by the Navier–Stokes equations. Prime examples are fluid–solid systems that involve multi-phase and/or multi-component flows, liquid crystals or micropolar fluids. These are just some examples of a broad class of fluids typically referred to as *complex fluids* [28]. One of the areas that could potentially benefit from accurate and efficient computational methods for the interaction of complex fluids and solids is that of mechanobiology. Just as an example, phenomena as important as cellular migration [51] or even cellular division [50] seem to be controlled to a significant extent by mechanics, and it seems plausible that at cellular scale capillary forces and spontaneous polarizations need to be considered.

Here, we present our initial steps toward a computational method for the interaction of complex fluids and solids. To illustrate our ideas, we focus on a particular engineering application, namely, the implosion of solids that enclose a compressible fluid. Structures containing a compressible fluid at a pressure below the external pressure have the potential to collapse inwards. For example, an air-filled structure may suffer an implosive collapse when it is immersed underwater, due to the increase of the external pressure. This is just an example of implosion which has been addressed before in the literature [25, 26, 37, 41, 49, 80], and that may be modeled using classical fluid theories. However, the aforementioned mechanism is not the only one that can cause the

implosive collapse of a structure. For example, in the case of vapor-filled structures, thermal variations can make vapor transform into liquid, reducing the internal pressure. We will refer to this phenomenon as *phase-change-driven implosion*, and this will be the subject of the current paper. It is clear that to model phase-change-driven implosion the way we have defined it, we will need a complex-fluid theory in which the fluid can undergo phase transformations.

## 1.2 Fluid dynamics with phase changes

Our approach to phase transformation is based on the *diffuse-interface* of *phase-field* method. The diffuse-interface approach can be defined as an alternative to the classical *sharp-interface* description. In the sharp-interface theory, several partial-differential equations must be solved on the different phases and they are coupled through boundary conditions that hold on a moving, and a priori unknown, interface. Thus, this technique may result in mathematical models that require complex numerical treatment. The key idea of the diffuse interface method is to use a field, namely the phase field, which is defined on the entire computational domain, and is a marker of the location of the different phases. The phase field varies smoothly on the computational domain, and naturally produces thin layers which represent interfaces between phases. This conceptualization notably simplifies the numerics because the problem reduces to solving a partial-differential equation on a fixed and known domain. From the computational point of view, the main disadvantage of the phase-field approach is that it typically leads to higher-order partial-differential equations that are stiff in space and time, and produce thin layers which evolve dynamically over the computational domain. However, most of these computational challenges are being addressed [30, 32, 34, 44], and computational phase-field modeling is becoming a mature topic. Phase-field models have been widely used in the condensed matter physics [18, 27, 48, 79] and material science [13, 54] and are rapidly getting established in the engineering field [12, 31, 82]. In this paper, we employ a phase-field approach based on the Navier–Stokes–Korteweg (NSK) equations to describe the behavior of the fluid in the implosion problem. The NSK equations constitute the most widely accepted mathematical model for single-component, two-phase (liquid and gas) flows [33]. Thus, the NSK theory may be used to model fluid flows in which the fluid can evaporate and condensate naturally due to pressure and/or temperature variations. The NSK system is the result of several works. The contribution of Gibbs [29], Korteweg, van der Waals [81] and Dunn and Serrin [23] should be highlighted. The current form of the system has been known for several years, though very few numerical solutions can be found in the literature. Notable exceptions include [20, 33, 44].

## 1.3 Computational challenges

From the computational point of view, there are at least two significant challenges in the phase-change-driven implosion problem as compared to other FSI simulations. First, phase-change-driven implosions lead to a violent and rapid collapse of the structure with strong compressions and large deformations [40]. Strong implosions may also involve contact, plastic deformation, and fracture, although this is out of the scope of this paper. Second, the NSK theory is more difficult to treat numerically than classical Navier–Stokes equations due to the presence of thin interfaces that must be resolved by the computational mesh. We try to address these challenges by using Isogeometric Analysis (IGA) for the spatial discretization of the problem. IGA is a generalization of the finite element method that was introduced in [35] and further developed in [1, 2, 5, 15–17, 24, 57, 83]. The main idea of IGA is to use functions from computational geometry to represent both the solution and the domain of a boundary-value problem. The most frequently utilized functions are Non-Uniform Rational B-Splines (NURBS) which are widely used in computational geometry and design, and will also be used in this work for our simulations.

We feel that IGA successfully addresses the two computational challenges that we mentioned before. In particular, IGA has been shown to perform well under large structural deformations [11, 42]. Additionally, IGA has been successfully used in computational phase-field modeling. In fact, it was shown that the higher-order global continuity of NURBS leads to a more accurate and stable solution of the thin layers that naturally arise in the solution of phase-field theories [30]. Finally, IGA has been previously used to solve FSI problems with remarkable success [4–7].

# 2 Governing equations

## 2.1 Kinematics

Let us introduce a reference domain $\Omega_{\widehat{\boldsymbol{x}}}$ which is fixed in time, and whose points are parameterized by coordinates $\widehat{\boldsymbol{x}}$. The reference domain is arbitrary and may take on different interpretations. Let us define a mapping $\widehat{\boldsymbol{\phi}} : \Omega_{\widehat{\boldsymbol{x}}} \times ]0,T[ \to \Omega_t$, where $]0,T[$ is the time interval of interest. For each time $t \in ]0,T[$, the function $\widehat{\boldsymbol{\phi}}$ maps the reference domain $\Omega_{\widehat{\boldsymbol{x}}}$ into its spatial configuration at time $t$, namely $\Omega_t$. Let us call $\boldsymbol{x}$ the coordinates in the spatial configuration, such that $\Omega_t \ni \boldsymbol{x} = \widehat{\boldsymbol{\phi}}(\widehat{\boldsymbol{x}},t)$. In the following, we will also use the notation $\widehat{\boldsymbol{\phi}}_t(\widehat{\boldsymbol{x}}) = \widehat{\boldsymbol{\phi}}(\widehat{\boldsymbol{x}},t)$. Using the mapping $\widehat{\boldsymbol{\phi}}$, we can define the displacement of a point in the referential domain

$$\widehat{\boldsymbol{u}}(\widehat{\boldsymbol{x}},t) = \widehat{\boldsymbol{\phi}}(\widehat{\boldsymbol{x}},t) - \widehat{\boldsymbol{x}}, \tag{1}$$

and its velocity

$$\widehat{\boldsymbol{v}} = \frac{\partial \widehat{\boldsymbol{u}}}{\partial t}. \tag{2}$$

Let us also define the mapping $\boldsymbol{\phi} : \Omega_{\boldsymbol{X}} \times ]0, T[ \to \Omega_t$. For each time $t \in ]0, T[$, this mapping transforms each material particle $\boldsymbol{X}$ into its spatial coordinate at time $t$, that is, $\boldsymbol{x} = \boldsymbol{\phi}(\boldsymbol{X}, t)$. Note that due to the arbitrariness of the referential domain, the mapping $\boldsymbol{\phi}$ can be simply thought of as a particular case of $\widehat{\boldsymbol{\phi}}$, but each mapping will be employed for a different purpose in this work, so we will use different notations. From the mapping $\boldsymbol{\phi}$, we can define the deformation gradient $\boldsymbol{F} = \frac{\partial \boldsymbol{\phi}}{\partial \boldsymbol{X}}$, the particle displacement

$$\boldsymbol{u}(\boldsymbol{X}, t) = \boldsymbol{\phi}(\boldsymbol{X}, t) - \boldsymbol{X}, \tag{3}$$

and the particle velocity

$$\boldsymbol{v} = \frac{\partial \boldsymbol{\phi}}{\partial t} = \frac{\partial \boldsymbol{u}}{\partial t}. \tag{4}$$

In what follows, we will also make use of the Eulerian counterpart of the particle velocity $\boldsymbol{v}$, namely, $\boldsymbol{v} \circ \boldsymbol{\phi}^{-1}$. From now on, in most instances, we will only use one symbol to denote a physical quantity (velocity, in this case) even if the functions $\boldsymbol{v}$ and $\boldsymbol{v} \circ \boldsymbol{\phi}^{-1}$ are clearly different. To avoid ambiguity in our notation we will use subscripts to clarify how derivatives are to be understood. For example, we will use the notation $\frac{\partial \boldsymbol{u}}{\partial t}|_X$ (respectively, $\frac{\partial \boldsymbol{u}}{\partial t}|_{\widehat{x}}$) to indicate that the time derivative is taken by holding $\boldsymbol{X}$ (respectively, $\widehat{\boldsymbol{x}}$) fixed. When neither $|_X$ nor $|_{\widehat{x}}$ are used in the time derivative, it is assumed to be taken by holding $\boldsymbol{x}$ fixed. We use a similar convention for spatial derivatives. For example, we denote by $\nabla$ the gradient with respect to the spatial coordinates $\boldsymbol{x}$. If coordinates other than $\boldsymbol{x}$ are used, the gradient operator will be assigned the appropriate subscript.

## 2.2 Governing equations of solid mechanics

The equations governing the structural dynamics will be presented in Lagrangian description, therefore all quantities are derived from the mapping $\boldsymbol{\phi}$. The deformation gradient takes on the form $\boldsymbol{F} = \boldsymbol{I} + \nabla_X \boldsymbol{u}$, where $\boldsymbol{I}$ denotes the identity tensor. We will also make use of the Cauchy–Green deformation tensor $\boldsymbol{C} = \boldsymbol{F}^T \boldsymbol{F}$, and the Green–Lagrange strain tensor $\boldsymbol{E} = (\boldsymbol{C} - \boldsymbol{I})/2$. The momentum balance in Lagrangian form can be written as

$$\rho_0^s \frac{\partial^2 \boldsymbol{u}}{\partial t^2}\bigg|_X = \nabla_X \cdot \boldsymbol{P} + \rho_0^s \boldsymbol{f}^s, \tag{5}$$

where $\rho_0^s$ is the mass density in the initial configuration, $\boldsymbol{f}^s$ represents body forces per unit mass, and $\boldsymbol{P}$ is the first Piola–Kirchhoff stress tensor. To define $\boldsymbol{P}$, we need to introduce a constitutive theory. We will use a hyperelastic model, therefore, the material behavior is described by a stored elastic energy density per unit volume of the undeformed configuration $W$. In particular, we will use the generalized neo-Hookean model with dilatational penalty proposed in [52], which is defined by

$$W = \frac{\mu}{2}\left(J^{-2/d}\mathrm{tr}(\boldsymbol{C}) - d\right) + \frac{\kappa}{2}\left(\frac{1}{2}\left(J^2 - 1\right) - \ln J\right), \tag{6}$$

where $d$ is the number of spatial dimensions, $\kappa$ and $\mu$ are the material bulk and shear moduli; $\mathrm{tr}(\cdot)$ denotes the trace operator and $J = \det(\boldsymbol{F})$. Note that in Eq. (6), the $\ln J$ term stabilizes the equation for the regime of strong compression, while the $J^2 - 1$ term penalizes the deviation of the Jacobian from unity. The second Piola–Kirchhoff stress tensor can be computed from $W$ as

$$\boldsymbol{S} = \frac{\partial W}{\partial \boldsymbol{E}} = \mu J^{-2/d}\left(\boldsymbol{I} - \frac{1}{d}\mathrm{tr}(\boldsymbol{C})\boldsymbol{C}^{-1}\right) + \frac{\kappa}{2}\left(J^2 - 1\right)\boldsymbol{C}^{-1}. \tag{7}$$

The first Piola–Kirchhoff stress tensor is simply defined as $\boldsymbol{P} = \boldsymbol{F}\boldsymbol{S}$. For future reference, we define the solid Cauchy stress tensor as

$$\boldsymbol{\sigma}^s = J^{-1}\boldsymbol{F}\boldsymbol{S}\boldsymbol{F}^T = J^{-1}\boldsymbol{P}\boldsymbol{F}^T. \tag{8}$$

## 2.3 Governing equations of fluid mechanics

In our model, the fluid dynamics is governed by the NSK equations, which account for mass, momentum and energy conservation. The NSK equations allow for liquid-gas and gas-liquid phase transformations, which can happen spontaneously without precursors. In the Eulerian frame, the NSK equations are given by

$$\frac{\partial \rho}{\partial t} + \nabla \cdot (\rho \boldsymbol{v}) = 0, \tag{9a}$$

$$\frac{\partial (\rho \boldsymbol{v})}{\partial t} + \nabla \cdot (\rho \boldsymbol{v} \otimes \boldsymbol{v}) - \nabla \cdot \boldsymbol{\sigma}^f - \rho \boldsymbol{f} = 0, \tag{9b}$$

$$\frac{\partial (\rho s)}{\partial t} + \nabla \cdot (\rho s \boldsymbol{v}) + \nabla \cdot \left(\frac{\boldsymbol{q}}{\theta}\right) = \mathscr{P}, \tag{9c}$$

where $s$ is the entropy density and the entropy production $\mathscr{P}$ depends on the fluid constitutive theory described later in the paper. The rest of the notation is as follows: $\rho$ is the density, $\boldsymbol{v}$ is the velocity vector, and $\otimes$ denotes the usual vector outer product; $\boldsymbol{\sigma}^f$ is the fluid stress tensor and $\boldsymbol{f}$ represents body forces per unit mass; $s$ is the entropy density, $\theta$ the temperature, and $\boldsymbol{q}$ the heat flux. Notice that to completely define the NSK equations, we need constitutive equations for the stress tensor and the heat flux, as well as a thermodynamic potential from which we can derive the state variables.

### 2.3.1 Stress tensor

The fluid Cauchy stress tensor $\boldsymbol{\sigma}^f$ is given by

$$\boldsymbol{\sigma}^f = \boldsymbol{\tau} - p\boldsymbol{I} + \boldsymbol{\varsigma}, \tag{10}$$

where $p$ is the pressure, $\boldsymbol{\tau}$ is the viscous stress tensor, and $\boldsymbol{\varsigma}$ denotes the so-called Korteweg tensor. We consider Newtonian fluids, therefore, the viscous stress tensor is defined as

$$\boldsymbol{\tau} = \bar{\mu}\left(\nabla\boldsymbol{v} + \nabla^T\boldsymbol{v}\right) + \bar{\lambda}\nabla\cdot\boldsymbol{v}\boldsymbol{I}, \tag{11}$$

where $\bar{\mu}$ and $\bar{\lambda}$ are the viscosity coefficients. Throughout this paper, we will assume that the Stokes hypothesis is satisfied, that is, $\bar{\lambda} = -2\bar{\mu}/3$. The Korteweg tensor is defined by the expression

$$\boldsymbol{\varsigma} = \lambda\left(\rho\Delta\rho + \frac{1}{2}|\nabla\rho|^2\right)\boldsymbol{I} - \lambda\nabla\rho\otimes\nabla\rho, \tag{12}$$

where $\lambda > 0$ is the capillarity coefficient, and $|\cdot|$ denotes the Euclidean norm of a vector. The Korteweg tensor gives rise to capillary forces which are withstood by gas-liquid interfaces. Note also that since $\boldsymbol{\varsigma}$ depends upon $\Delta\rho$, the linear momentum balance equation includes third-order partial differential operators.

### 2.3.2 Heat conduction

We use the isotropic Fourier law, that is, $\boldsymbol{q} = -k\nabla\theta$, where $k$ is the thermal conductivity.

### 2.3.3 Entropy production

With the above-presented constitutive theory, the entropy production $\mathscr{P}$ takes on the form

$$\mathscr{P} = k\frac{1}{\theta^2}|\nabla\theta|^2 + \frac{1}{\theta}\boldsymbol{\tau}:\nabla\boldsymbol{v} + \frac{\rho r}{\theta} + \frac{\rho\boldsymbol{f}\cdot\boldsymbol{v}}{\theta}, \tag{13}$$

where $r$ is the heat supply per unit mass.

### 2.3.4 State variables

The NSK theory fits into classical thermodynamics, and as a consequence, state variables can be derived from a Helmholtz free-energy potential. To allow for phase transformations in the fluid, we do not use the classical Helmholtz free-energy of a perfect gas, but that of a so-called van der Waals fluid [20, 43]. The peculiarity of the van der Waals Helmholtz free-energy is that it may be non-convex for low temperatures, allowing for spontaneous phase changes. Using the van der Waals–Helmholtz free-energy and standard thermodynamics [43], we obtain the pressure as

$$p = Rb\left(\frac{\rho\theta}{b-\rho}\right) - a\rho^2, \tag{14}$$

which is known as van der Waals equation. In Eq. (14), $R$ is the specific gas constant, while $a$ and $b$ are positive constants. Also from the Helmholtz free-energy, we can obtain the entropy density as

$$s = -R\log\left(\frac{\rho}{b-\rho}\right) + c_v\log\left(\frac{\theta}{\theta_c}\right) \tag{15}$$

where $c_v$ is the specific heat capacity and $\theta_c$ is a reference temperature to be defined later. In the NSK theory, phase transformations are naturally accommodated without introducing additional fields, and without precursors. The density itself is a marker of the vapor and liquid phases (see [33]). To give a precise definition of the phases, let us consider $\theta$ a parameter in Eq. (14). Fig. 1 shows a non-dimensional plot of the pressure as a function of density for different values of $\theta$. We observe qualitatively different behaviors for $\theta > \theta_c$, and $\theta < \theta_c$, where

$$\theta_c = \frac{8}{27}\frac{ab}{R} \tag{16}$$

is the so-called critical temperature. For $\theta > \theta_c$, $p$ is a monotonic function of $\rho$, the gaseous phase is stable and the liquid phase is unstable (not proven here). For $\theta < \theta_c$, there is a density interval, namely $(\rho_v, \rho_l)$, in which $\partial p/\partial\rho < 0$, and as a consequence, there may be stable co-existence of gas and liquid. In this temperature range, the gaseous phase is defined by $\rho \in (0, \rho_v)$, while the liquid phase is defined by $\rho \in (\rho_l, b)$. The region $\rho \in (\rho_v, \rho_l)$ has no physical meaning, but in the NSK theory, may be interpreted as a smooth interface between the vapor and liquid phases which spans over a length scale $\sqrt{\lambda/a}$. Note also that in the inviscid, non-conducting limit, the NSK equations are ill-posed for $\lambda = 0$, and capillary forces are necessary to restore well-posedness. For further details on the NSK equations, the reader is referred to [33, 43].

**Remark** Note that our model neglects the thermal physics in the solid. Although it would be straightforward to consider a thermo-elastic theory, we believe that it is not a key ingredient for the objectives of this paper.

## 3 Numerical formulation

In this section we propose FSI algorithms to solve the implosion problem. Our methods extend those presented in [4] to the realm of complex fluids.

### 3.1 Computational framework

In our model, the structure is treated as a nonlinear hyperelastic solid in Lagrangian description. The fluid is a complex, viscous and compressible fluid, governed by the NSK
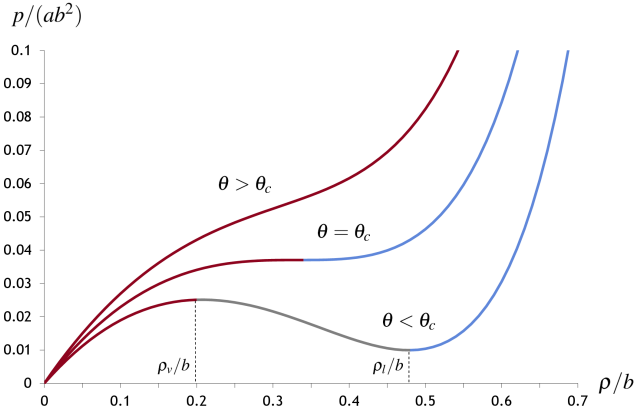
**Fig. 1** Non-dimensional plot of van der Waals pressure as a function of density. The pressure is a non-monotone function of density for $\theta < \theta_c$. For comparison purposes, we note that for a given temperature, the pressure-density law of a perfect gas, would be a straight line tangent to the van der Waals curve at $\rho = 0$.

theory. The NSK equations hold on a moving domain, and heretofore, have been presented in Eulerian description. From a computational viewpoint, we aim at using a semidiscrete algorithm in which space discretization is performed using IGA, and time discretization is carried out by a finite-difference-type method. Eulerian descriptions are not well-suited for semidiscretized methods on moving domains, so we will use the Arbitrary Lagrangian-Eulerian (ALE) formulation [21, 22, 36]. In ALE methods the partial time and space derivatives employed in the balance equations are taken with respect to different domains, namely, the reference and the current domain. This particularity allows for a straightforward use of semi-discrete methods, even when the equations are posed on a moving domain [4].

Using the techniques presented in [9,22], the NSK system in the ALE description may be written as:

$$\left.\frac{\partial \rho}{\partial t}\right|_{\widehat{x}} + (\boldsymbol{v} - \widehat{\boldsymbol{v}}) \cdot \nabla \rho + \rho \nabla \cdot \boldsymbol{v} = 0, \tag{17a}$$

$$\rho \left.\frac{\partial \boldsymbol{v}}{\partial t}\right|_{\widehat{x}} + \rho (\boldsymbol{v} - \widehat{\boldsymbol{v}}) \cdot \nabla \boldsymbol{v} - \nabla \cdot \boldsymbol{\sigma}^f - \rho \boldsymbol{f} = 0, \tag{17b}$$

$$\left.\frac{\partial (\rho s)}{\partial t}\right|_{\widehat{x}} + (\boldsymbol{v} - \widehat{\boldsymbol{v}}) \cdot \nabla (\rho s) + \rho s \nabla \cdot \boldsymbol{v} + \nabla \cdot \left(\frac{\boldsymbol{q}}{\theta}\right) = \mathscr{P}, \tag{17c}$$

where $\widehat{\boldsymbol{v}}$ is the fluid domain velocity [4], which is associated to the mapping $\widehat{\boldsymbol{\phi}}$ that transforms the referential domain into the spatial configuration. The details of the mapping $\widehat{\boldsymbol{\phi}}$ will be will be provided later in the paper.

**Remark** For moving domain applications, the Eulerian form of the NSK equations may be discretized using a space–time technique, an alternative to the ALE approach. See references [9,10,56,59–62,65,67–69,71] for recent advances in space–time methods for fluid mechanics and FSI.
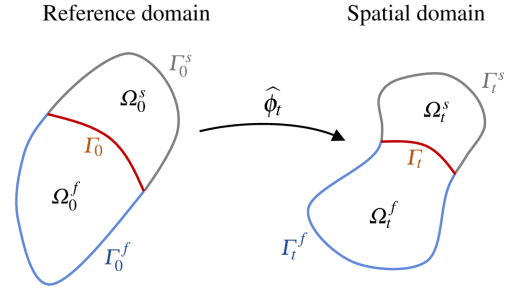


**Fig. 2** Fluid and solid subdomains in the reference and spatial configuration.

### 3.2 Definition of the computational domain

Let $\Omega_0$ denote the initial configuration of the entire domain of the problem, that is, the fluid and solid domains combined. $\Omega_0$ will be adopted as the reference configuration and also as material configuration. We may decompose $\Omega_0$ as

$$\Omega_0 = \overline{\Omega_0^f \cup \Omega_0^s}, \qquad \text{with} \qquad \Omega_0^f \cap \Omega_0^s = \emptyset, \tag{18}$$

where superscripts $s$ and $f$ refer to the solid and the fluid domain, respectively. We may also decompose the spatial configuration of $\Omega_0$ at time $t$, namely $\Omega_t$, as

$$\Omega_t = \overline{\Omega_t^f \cup \Omega_t^s}, \qquad \text{with} \qquad \Omega_t^f \cap \Omega_t^s = \emptyset. \tag{19}$$

Let $\Gamma_0$ and $\Gamma_t$ be the fluid-solid interface where the subscripts 0 and $t$ denote the initial and the current configuration, respectively. We will denote by $\Gamma_0^s$ and $\Gamma_t^s$ the boundary of the solid subdomain without the part of the fluid-structure interface. Likewise, $\Gamma_0^f$ and $\Gamma_t^f$ denote the boundary of the fluid subdomain without the fluid-structure interface. See Fig. 2 for an illustration.

### 3.3 Continuous problem in the weak form

#### 3.3.1 Solid mechanics problem

To define the weak form of the solid problem we need to consider suitable boundary conditions. Let us assume that the solid boundary $\Gamma_0^s$ can be decomposed into Neumann and Dirichlet parts denoted by $(\Gamma_0^s)_N$ and $(\Gamma_0^s)_D$, respectively. Note that this splitting may be different for each spatial direction, although this is not explicitly indicated in our notation. Let us define a trial solution functional space $\mathscr{X}^s = \mathscr{X}^s(\Omega_0^s)$ whose members verify the Dirichlet boundary conditions of the problem, and a weighting function space $\mathscr{Y}^s = \mathscr{Y}^s(\Omega_0^s)$ which is identical to $\mathscr{X}^s$, but verifies homogeneous conditions on $(\Gamma_0^s)_D$. The variational formulation can be stated as follows: Find $\boldsymbol{u} \in \mathscr{X}^s$ such that $\forall \boldsymbol{w}^s \in \mathscr{Y}^s$,

$$B^s(\boldsymbol{w}^s, \boldsymbol{u}) = F^s(\boldsymbol{w}^s), \tag{20}$$

where

$$B^s(\boldsymbol{w}^s, \boldsymbol{u}) = \int_{\Omega_0^s} \left( \boldsymbol{w}^s \cdot \rho_0^s \frac{\partial^2 \boldsymbol{u}}{\partial t^2} \bigg|_X + \nabla_X \boldsymbol{w}^s : \boldsymbol{P} \right) \mathrm{d}\Omega_0^s \qquad (21)$$

and

$$F^s(\boldsymbol{w}^s) = \int_{\Omega_0^s} \boldsymbol{w}^s \cdot \rho_0^s \boldsymbol{f}^s \mathrm{d}\Omega_0^s + \int_{(\Gamma_0^s)_N} \boldsymbol{w}^s \cdot \widehat{\boldsymbol{h}} \mathrm{d}(\Gamma_0^s)_N. \qquad (22)$$

Note that this variational formulation weakly enforces Eq. (5), and the Neumman boundary condition $\boldsymbol{P}\widehat{\boldsymbol{n}}^s = \widehat{\boldsymbol{h}}$ on $(\Gamma_0^s)_N$. Here, $\widehat{\boldsymbol{h}}$ is a given traction and $\widehat{\boldsymbol{n}}^s$ is the unit outward normal to the solid boundary in the referential domain. For future reference, we note that the boundary condition corresponding to a follower load $\mathrm{p}$ in the direction of the inner normal to the solid boundary may be imposed by taking $\widehat{\boldsymbol{h}} = -\mathrm{p}J\boldsymbol{F}^{-T}\widehat{\boldsymbol{n}}^s$.

### 3.3.2 Fluid mechanics problem

To derive our weak form we need to specify suitable boundary conditions. For the time being, we will focus on solid-wall boundary conditions. In classical compressible gas dynamics, solid-wall boundary conditions may be imposed, for example, by setting velocity and temperature to given values. This is not sufficient to get a well-posed boundary value problem for the NSK equations, due to the third-order spatial derivative of the density in the linear momentum balance. To attain well-posedness, the boundary condition

$$\nabla\rho \cdot \boldsymbol{n}^f = -|\nabla\rho|\cos(\varphi) \qquad (23)$$

may be imposed. Here, $\boldsymbol{n}^f$ denotes the unit outward normal to the fluid boundary, and $\varphi$ is the contact angle between the liquid-vapor interface and the solid, measured in the vapor phase. Let us also mention that to derive our weak form, we will split the momentum balance equation (17b) into two lower-order equations by introducing a new variable defined as $\Upsilon = \Delta\rho$. Notice that this step is not necessary with isogeometric analysis since IGA allows to use the globally $C^1$-continuous basis functions that are required to approximate the NSK equations in primal form (see [33]). However, to allow for the use of classical $C^0$ finite elements, and to simplify the imposition of the boundary condition (23), we chose to use the split form. Let us introduce the trial solution space $\mathscr{X}^f = \mathscr{X}^f(\Omega_t^f)$ whose members satisfy all Dirichlet boundary conditions. The weighting functions space $\mathscr{Y}^f = \mathscr{Y}^f(\Omega_t^f)$ is identical to $\mathscr{X}^f$, but all restrictions on the Dirichlet boundary are homogeneous. The variational formulation is stated as follows: Find $\boldsymbol{U} = \{\rho, \boldsymbol{v}, \Upsilon, \theta\} \in \mathscr{X}^f$ such that $\forall \boldsymbol{W} = \{w^1, \boldsymbol{w}^2, w^3, w^4\} \in \mathscr{Y}^f$,

$$B^f(\boldsymbol{W}, \boldsymbol{U}; \widehat{\boldsymbol{v}}) = 0, \qquad (24)$$

where

$$\begin{aligned}
B^f(\boldsymbol{W}, \boldsymbol{U}; \widehat{\boldsymbol{v}}) = &\int_{\Omega_t^f} w^1 \left( \frac{\partial\rho}{\partial t} \bigg|_{\widehat{x}} + (\boldsymbol{v} - \widehat{\boldsymbol{v}}) \cdot \nabla\rho + \rho\nabla \cdot \boldsymbol{v} \right) \mathrm{d}\Omega_t^f \\
&+ \int_{\Omega_t^f} \boldsymbol{w}^2 \cdot \left( \rho \frac{\partial\boldsymbol{v}}{\partial t} \bigg|_{\widehat{x}} + \rho(\boldsymbol{v} - \widehat{\boldsymbol{v}}) \cdot \nabla\boldsymbol{v} - \rho\boldsymbol{f} \right) \mathrm{d}\Omega_t^f \\
&+ \int_{\Omega_t^f} \nabla\boldsymbol{w}^2 : (\boldsymbol{\tau} - p\boldsymbol{I}) \mathrm{d}\Omega_t^f \\
&+ \int_{\Omega_t^f} \nabla \cdot \boldsymbol{w}^2 \lambda \left( \rho\Upsilon + \frac{1}{2}|\nabla\rho|^2 \right) \mathrm{d}\Omega_t^f \\
&- \int_{\Omega_t^f} \nabla\boldsymbol{w}^2 : \lambda\nabla\rho \otimes \nabla\rho \mathrm{d}\Omega_t^f \\
&+ \int_{\Omega_t^f} w^3\Upsilon \mathrm{d}\Omega_t^f + \int_{\Omega_t^f} \nabla w^3 \cdot \nabla\rho \mathrm{d}\Omega_t^f \\
&+ \int_{\Gamma_t^f \cup \Gamma_t} w^3 |\nabla\rho|\cos(\varphi) \mathrm{d}(\Gamma_t^f \cup \Gamma_t) \\
&+ \int_{\Omega_t^f} w^4 \left( \frac{\partial(\rho s)}{\partial t} \bigg|_{\widehat{x}} + (\boldsymbol{v} - \widehat{\boldsymbol{v}}) \cdot \nabla(\rho s) \right) \mathrm{d}\Omega_t^f \\
&+ \int_{\Omega_t^f} w^4 \left( \rho s\nabla \cdot \boldsymbol{v} - \frac{1}{\theta}\boldsymbol{\tau} : \nabla\boldsymbol{v} - k\frac{1}{\theta^2}|\nabla\theta|^2 \right) \mathrm{d}\Omega_t^f \\
&- \int_{\Omega_t^f} w^4 \left( \frac{\rho r}{\theta} + \frac{\rho\boldsymbol{f} \cdot \boldsymbol{v}}{\theta} \right) \mathrm{d}\Omega_t^f \\
&- \int_{\Omega_t^f} \nabla w^4 \cdot \frac{\boldsymbol{q}}{\theta} \mathrm{d}\Omega_t^f. \qquad (25)
\end{aligned}$$

Note that the variational formulation (24)–(25) weakly imposes the NSK equations and the boundary condition (23). If Dirichlet boundary conditions are not set on the entire boundary for velocity or temperature, then the variational formulation weakly imposes the conjugate stress-free condition or vanishing heat flux at the wall.

### 3.3.3 Fluid domain motion

The goal of this motion is to produce a smooth evolution of the fluid domain given the displacement data on the fluid–solid interface. This motion will be associated to the mapping $\widehat{\boldsymbol{\phi}}$, and will be understood as a succession of fictitious linear elastic boundary-value problems [4,39,53,73–76]. Let us use the notation $\widehat{\boldsymbol{\phi}}_t(\widehat{\boldsymbol{x}}) = \widehat{\boldsymbol{\phi}}(\widehat{\boldsymbol{x}}, t)$. We may define the displacement of the reference domain at time $t$ as

$$\widehat{\boldsymbol{u}}_t(\widehat{\boldsymbol{x}}) = \widehat{\boldsymbol{u}}(\widehat{\boldsymbol{x}}, t) = \widehat{\boldsymbol{\phi}}(\widehat{\boldsymbol{x}}, t) - \widehat{\boldsymbol{x}}. \qquad (26)$$

The function $\widehat{\boldsymbol{\phi}}_{\widetilde{t}}$ is the analogue of $\widehat{\boldsymbol{\phi}}_t$ at time $\widetilde{t}$, and $\widehat{\boldsymbol{u}}_t \circ \widehat{\boldsymbol{\phi}}_{\widetilde{t}}^{-1}$ is simply the displacement of the reference domain at time $t$ with respect to the configuration of the reference domain at time $\widetilde{t}$. Here, we understand $\widetilde{t} < t$ as a time instant close to $t$, which in a time-discrete context is usually the final configuration of the previous time step. To determine $\widehat{\boldsymbol{\phi}}_t$, and thus, the motion of the fluid subdomain, we use the identity

$$\widehat{\boldsymbol{\phi}}_t(\widehat{\boldsymbol{x}}) = \widehat{\boldsymbol{\phi}}_{\widetilde{t}}(\widehat{\boldsymbol{x}}) + \left( \widehat{\boldsymbol{u}}_t \circ \widehat{\boldsymbol{\phi}}_{\widetilde{t}}^{-1} \right) \left( \widehat{\boldsymbol{\phi}}_{\widetilde{t}}(\widehat{\boldsymbol{x}}) \right), \qquad (27)$$

where $\widehat{\boldsymbol{u}}_t \circ \widehat{\boldsymbol{\phi}}_{\tilde{t}}^{-1}$ is obtained from a linear elastic boundary-value problem. Let us call $\boldsymbol{u}^m$ our "approximation" of $\widehat{\boldsymbol{u}}_t \circ \widehat{\boldsymbol{\phi}}_{\tilde{t}}^{-1}$ obtained by solving a fictitious linear-elastic boundary value problem. The unknown $\boldsymbol{u}^m$ is subject to Dirichlet boundary conditions $\boldsymbol{u}^m = \boldsymbol{u}_t \circ \widehat{\boldsymbol{\phi}}_{\tilde{t}}^{-1}$ on $\Gamma_{\tilde{t}}$, where $\boldsymbol{u}_t$ is the particle displacement at time $t$. These Dirichlet boundary conditions are strongly built into the trial solution space $\mathscr{V}^m = \mathscr{V}^m(\Omega_{\tilde{t}}^f)$. The corresponding weighting function space, satisfying homogeneous conditions on the boundary, is denoted by $\mathscr{W}^m = \mathscr{W}^m(\Omega_{\tilde{t}}^f)$. The variational formulation can be stated as follows: Find $\boldsymbol{u}^m \in \mathscr{V}^m$ such that $\forall \boldsymbol{w}^m \in \mathscr{W}^m$,

$$B^m(\boldsymbol{w}^m, \boldsymbol{u}^m) = 0, \tag{28}$$

where

$$B^m(\boldsymbol{w}^m, \boldsymbol{u}^m) = \int_{\Omega_{\tilde{t}}^f} \nabla_{\tilde{x}}^{sym} \boldsymbol{w}^m : 2\mu^m \nabla_{\tilde{x}}^{sym} \boldsymbol{u}^m \mathrm{d}\Omega_{\tilde{t}}^f$$
$$+ \int_{\Omega_{\tilde{t}}^f} \nabla_{\tilde{x}} \cdot \boldsymbol{w}^m \lambda^m \nabla_{\tilde{x}} \cdot \boldsymbol{u}^m \mathrm{d}\Omega_{\tilde{t}}^f, \tag{29}$$

while $\mu^m$ and $\lambda^m$ are the Lamé parameters of the fictitious elastic model characterizing the motion of the fluid domain; $\nabla_{\tilde{x}}$ is the gradient operator on $\Omega_{\tilde{t}}$ and $\nabla_{\tilde{x}}^{sym}$ is its symmetric part. Once $\boldsymbol{u}^m$ has been determined, the ALE mapping in the fluid subdomain can be obtained from Eq. (27) by replacing $\widehat{\boldsymbol{u}}_t \circ \widehat{\boldsymbol{\phi}}_{\tilde{t}}^{-1}$ with $\boldsymbol{u}^m$.

### 3.3.4 Coupled FSI problem

Here, we present the coupled fluid-structure interaction problem. The variational formulation of the problem is stated as follows: Find $\boldsymbol{U} = \{\rho, \boldsymbol{v}, \Upsilon, \theta\} \in \mathscr{X}^f$, $\boldsymbol{u} \in \mathscr{X}^s$ and $\boldsymbol{u}^m \in \mathscr{V}^m$ such that $\forall \boldsymbol{W} = \{w^1, \boldsymbol{w}^2, w^3, w^4\} \in \mathscr{Y}^f$, $\forall \boldsymbol{w}^s \in \mathscr{Y}^s$ and $\forall \boldsymbol{w}^m \in \mathscr{W}^m$,

$$B^f(\boldsymbol{W}, \boldsymbol{U}; \widehat{\boldsymbol{v}}) + B^s(\boldsymbol{w}^s, \boldsymbol{u}) + B^m(\boldsymbol{w}^m, \boldsymbol{u}^m) = F^s(\boldsymbol{w}^s), \tag{30}$$

with the following fluid-solid interface conditions:

$$\boldsymbol{v} = \frac{\partial \boldsymbol{u}}{\partial t} \circ \widehat{\boldsymbol{\phi}}^{-1} \quad \text{on} \quad \Gamma_t, \tag{31}$$

$$\boldsymbol{w}^2 = \boldsymbol{w}^s \circ \widehat{\boldsymbol{\phi}}^{-1} \quad \text{on} \quad \Gamma_t. \tag{32}$$

In (30), $\widehat{\boldsymbol{v}}$ is obtained from $\widehat{\boldsymbol{\phi}}$ which is determined as explained in Sect. 3.3.3. Note also that Eq. (31) ensures strong kinematical compatibility at the fluid-structure interface. Eq. (32) leads to a weak enforcement of traction compatibility at the interface, which in the spatial configuration may be expressed as $\boldsymbol{\sigma}^f \boldsymbol{n}^f + \boldsymbol{\sigma}^s \boldsymbol{n}^s = 0$ on $\Gamma_t$, where $\boldsymbol{n}^s$ is the unit outward normal to the solid in the spatial configuration.

### 3.4 Semidiscrete formulation

For the spatial discretization of the coupled problem we make use of NURBS-based isogeometric analysis. We define finite-dimensional approximations of the funtional spaces, namely, $\mathscr{X}_h^f$, $\mathscr{X}_h^s$ and $\mathscr{V}_h^m$ such that $\mathscr{X}_h^f \subset \mathscr{X}^f$, $\mathscr{X}_h^s \subset \mathscr{X}^s$, and $\mathscr{V}_h^m \subset \mathscr{V}^m$. Analogously, we introduce $\mathscr{Y}_h^f \subset \mathscr{Y}^f$, $\mathscr{Y}_h^s \subset \mathscr{Y}^s$, and $\mathscr{W}_h^m \subset \mathscr{W}^m$. We approximate (30) by the following variational problem over the finite element spaces: Find $\boldsymbol{U}_h = \{\rho_h, \boldsymbol{v}_h, \Upsilon_h, \theta_h\} \in \mathscr{X}_h^f$, $\boldsymbol{u}_h \in \mathscr{X}_h^s$ and $\boldsymbol{u}_h^m \in \mathscr{V}_h^m$ such that $\forall \boldsymbol{W}_h = \{w_h^1, \boldsymbol{w}_h^2, w_h^3, w_h^4\} \in \mathscr{Y}_h^f$, $\forall \boldsymbol{w}_h^s \in \mathscr{Y}_h^s$ and $\forall \boldsymbol{w}_h^m \in \mathscr{W}_h^m$,

$$B^f(\boldsymbol{W}_h, \boldsymbol{U}_h; \widehat{\boldsymbol{v}}_h) + B^s(\boldsymbol{w}_h^s, \boldsymbol{u}_h) + B^m(\boldsymbol{w}_h^m, \boldsymbol{u}_h^m) = F^s(\boldsymbol{w}_h^s), \tag{33}$$

where

$$\rho_h(\boldsymbol{x}, t) = \sum_{A \in I_f} \rho_A(t) N_A(\boldsymbol{x}, t), \qquad w_h^1(\boldsymbol{x}, t) = \sum_{A \in I_f} w_A^1 N_A(\boldsymbol{x}, t), \tag{34a}$$

$$\boldsymbol{u}_h(\boldsymbol{X}, t) = \sum_{A \in I_s} \boldsymbol{u}_A(t) \widehat{N}_A(\boldsymbol{X}), \qquad \boldsymbol{w}_h^s(\boldsymbol{X}) = \sum_{A \in I_s} \boldsymbol{w}_A^s \widehat{N}_A(\boldsymbol{X}), \tag{34b}$$

$$\boldsymbol{u}_h^m(\tilde{\boldsymbol{x}}, \tilde{t}) = \sum_{A \in I_f} \widehat{\boldsymbol{u}}_A(\tilde{t}) \tilde{N}_A(\tilde{\boldsymbol{x}}, \tilde{t}), \qquad \boldsymbol{w}_h^m(\tilde{\boldsymbol{x}}, \tilde{t}) = \sum_{A \in I_f} \boldsymbol{w}_A^m \tilde{N}_A(\tilde{\boldsymbol{x}}, \tilde{t}), \tag{34c}$$

while the discrete fluid mesh velocity in the spatial configuration is given by

$$\widehat{\boldsymbol{v}}_h(\boldsymbol{x}, t) = \sum_{A \in I_f} \frac{\partial \widehat{\boldsymbol{u}}_A}{\partial t}(t) N_A(\boldsymbol{x}, t). \tag{35}$$

The variables $\boldsymbol{v}_h$, $\Upsilon_h$ and $\theta_h$ are defined analogously to $\rho_h$, while $\boldsymbol{w}_h^2$, $w_h^3$ and $w_h^4$ are defined similarly to $w_h^1$. In Eqs. (34), the $\widehat{N}_A$'s are a set of basis functions defined on $\Omega_0$ and $I_s$ is their global-index set. The $\widehat{N}_A$'s are fixed in time and have square integrable first spatial derivatives. Their continuity can be arbitrarily high inside the solid and fluid subdomains, but they are exactly $\mathscr{C}^0$ on $\Gamma_0$ (in the normal direction). $N_A$ is the push forward of $\widehat{N}_A$ to the spatial domain $\Omega_t$, that is, $N_A(\boldsymbol{x}, t) = \widehat{N}_A \circ \widetilde{\boldsymbol{\phi}^h}^{-1}(\boldsymbol{x}, t)$, where $\widetilde{\boldsymbol{\phi}^h}^{-1}$ is the discrete counterpart of $\widehat{\boldsymbol{\phi}}^{-1}$. Likewise, $\tilde{N}_A$ is the push forward of $\widehat{N}_A$ to the spatial domain at time $\tilde{t}$ (see Sect. 3.3.3), i.e., $\tilde{N}_A(\tilde{\boldsymbol{x}}, \tilde{t}) = \widehat{N}_A \circ \widetilde{\boldsymbol{\phi}^h}^{-1}(\tilde{\boldsymbol{x}}, \tilde{t})$. $I_f$ is the global-index set of the $N_A$'s.

In order to ensure a correct coupling between the fluid and solid, we must enforce the compatibility of kinematics and tractions at the fluid–structure interface $\Gamma_t$. To do so, we use a unique set of trial functions for the velocity degrees-of-freedom, and the corresponding test functions for the linear momentum equations at the fluid–structure interface. This

leads to a typical monolithic FSI formulation with a matching interface discretization, and gives strong (pointwise) satisfaction of the kinematics, and weak satisfaction of the traction compatibility conditions.

## 3.5 Time discretization and numerical implementation

We integrate the FSI equations in time using the generalized-$\alpha$ method. This method was originally proposed by Chung and Hulbert [14] for the equations of structural dynamics, and successfully applied in the context of turbulence simulation [3,38] and phase-field modeling [30,33].

### 3.5.1 Time stepping scheme

Let $\boldsymbol{U}$, $\dot{\boldsymbol{U}}$, $\ddot{\boldsymbol{U}}$ denote the vectors of control variable degrees of freedom of the fluid-structure system, and its first and second time derivatives, respectively. Let $\boldsymbol{V}$, $\dot{\boldsymbol{V}}$, $\ddot{\boldsymbol{V}}$ denote the vectors of control variable degrees of freedom of mesh displacements, velocities and accelerations. We define the residual vectors

$$\boldsymbol{R}^{cont} = \{R_A^{cont}\}, \tag{36a}$$
$$\boldsymbol{R}^{mom} = \{R_{A,i}^{mom}\}, \tag{36b}$$
$$\boldsymbol{R}^{aux} = \{R_A^{aux}\}, \tag{36c}$$
$$\boldsymbol{R}^{ener} = \{R_A^{ener}\}, \tag{36d}$$
$$\boldsymbol{R}^{mesh} = \{R_{A,i}^{mesh}\}, \tag{36e}$$

where $A$ is a control-variable index and $i$ is an index associated to the spatial dimensions. The residual components are defined as

$$R_A^{cont} = B^f(\{N_A, 0, 0, 0\}, \{\rho_h, \boldsymbol{v}_h, \Upsilon_h, \theta_h\}; \widehat{\boldsymbol{v}}_h), \tag{37a}$$
$$\begin{aligned} R_{A,i}^{mom} = {} & B^f(\{0, N_A\boldsymbol{e}_i, 0, 0\}, \{\rho_h, \boldsymbol{v}_h, \Upsilon_h, \theta_h\}; \widehat{\boldsymbol{v}}_h) \\ & + B^s(\widehat{N}_A\boldsymbol{e}_i, \boldsymbol{u}_h) - F^s(\widehat{N}_A\boldsymbol{e}_i), \end{aligned} \tag{37b}$$
$$R_A^{aux} = B^f(\{0, 0, N_A, 0\}, \{\rho_h, \boldsymbol{v}_h, \Upsilon_h, \theta_h\}; \widehat{\boldsymbol{v}}_h), \tag{37c}$$
$$R_A^{ener} = B^f(\{0, 0, 0, N_A\}, \{\rho_h, \boldsymbol{v}_h, \Upsilon_h, \theta_h\}; \widehat{\boldsymbol{v}}_h), \tag{37d}$$
$$R_{A,i}^{mesh} = B^m(\tilde{N}_A\boldsymbol{e}_i, \boldsymbol{u}_h^m), \tag{37e}$$

where $\boldsymbol{e}_i$ is the $i$th cartesian basis vector. Our time stepping scheme can be defined as follows: Given the discrete approximation to the global vectors of control variables at time $t_n$, namely, $\boldsymbol{U}_n, \dot{\boldsymbol{U}}_n, \ddot{\boldsymbol{U}}_n, \boldsymbol{V}_n, \dot{\boldsymbol{V}}_n, \ddot{\boldsymbol{V}}_n$ and the current time step $\Delta t = t_{n+1} - t_n$ find $\boldsymbol{U}_{n+1}, \dot{\boldsymbol{U}}_{n+1}, \ddot{\boldsymbol{U}}_{n+1}, \boldsymbol{V}_{n+1}, \dot{\boldsymbol{V}}_{n+1}, \ddot{\boldsymbol{V}}_{n+1}$

such that

$$\boldsymbol{R}^{cont}(\boldsymbol{U}_{n+\alpha_f}, \dot{\boldsymbol{U}}_{n+\alpha_f}, \ddot{\boldsymbol{U}}_{n+\alpha_m}, \boldsymbol{V}_{n+\alpha_f}, \dot{\boldsymbol{V}}_{n+\alpha_f}, \ddot{\boldsymbol{V}}_{n+\alpha_m}) = 0,$$
$$\boldsymbol{R}^{mom}(\boldsymbol{U}_{n+\alpha_f}, \dot{\boldsymbol{U}}_{n+\alpha_f}, \ddot{\boldsymbol{U}}_{n+\alpha_m}, \boldsymbol{V}_{n+\alpha_f}, \dot{\boldsymbol{V}}_{n+\alpha_f}, \ddot{\boldsymbol{V}}_{n+\alpha_m}) = 0,$$
$$\boldsymbol{R}^{aux}(\boldsymbol{U}_{n+\alpha_f}, \dot{\boldsymbol{U}}_{n+\alpha_f}, \ddot{\boldsymbol{U}}_{n+\alpha_m}, \boldsymbol{V}_{n+\alpha_f}, \dot{\boldsymbol{V}}_{n+\alpha_f}, \ddot{\boldsymbol{V}}_{n+\alpha_m}) = 0,$$
$$\boldsymbol{R}^{ener}(\boldsymbol{U}_{n+\alpha_f}, \dot{\boldsymbol{U}}_{n+\alpha_f}, \ddot{\boldsymbol{U}}_{n+\alpha_m}, \boldsymbol{V}_{n+\alpha_f}, \dot{\boldsymbol{V}}_{n+\alpha_f}, \ddot{\boldsymbol{V}}_{n+\alpha_m}) = 0,$$
$$\boldsymbol{R}^{mesh}(\boldsymbol{U}_{n+\alpha_f}, \dot{\boldsymbol{U}}_{n+\alpha_f}, \ddot{\boldsymbol{U}}_{n+\alpha_m}, \boldsymbol{V}_{n+\alpha_f}, \dot{\boldsymbol{V}}_{n+\alpha_f}, \ddot{\boldsymbol{V}}_{n+\alpha_m}) = 0, \tag{38}$$

$$\dot{\boldsymbol{U}}_{n+1} = \dot{\boldsymbol{U}}_n + \Delta t((1-\gamma)\ddot{\boldsymbol{U}}_n + \gamma\ddot{\boldsymbol{U}}_{n+1}),$$
$$\boldsymbol{U}_{n+1} = \boldsymbol{U}_n + \Delta t\dot{\boldsymbol{U}}_n + \frac{\Delta t^2}{2}\left((1-2\beta)\ddot{\boldsymbol{U}}_n + 2\beta\ddot{\boldsymbol{U}}_{n+1}\right),$$
$$\dot{\boldsymbol{V}}_{n+1} = \dot{\boldsymbol{V}}_n + \Delta t((1-\gamma)\ddot{\boldsymbol{V}}_n + \gamma\ddot{\boldsymbol{V}}_{n+1}),$$
$$\boldsymbol{V}_{n+1} = \boldsymbol{V}_n + \Delta t\dot{\boldsymbol{V}}_n + \frac{\Delta t^2}{2}\left((1-2\beta)\ddot{\boldsymbol{V}}_n + 2\beta\ddot{\boldsymbol{V}}_{n+1}\right), \tag{39}$$

where

$$\square_{n+\alpha_f} = \square_n + \alpha_f\left(\square_{n+1} - \square_n\right), \tag{40a}$$
$$\square_{n+\alpha_m} = \square_n + \alpha_m\left(\square_{n+1} - \square_n\right), \tag{40b}$$

and $\square$ denotes a generic control variable vector. Note that although $\boldsymbol{U}_{n+1}, \dot{\boldsymbol{U}}_{n+1}, \ddot{\boldsymbol{U}}_{n+1}$ are treated separately in the algorithm, they are not independent because they need to satisfy Eqns. (39). The same argument applies to $\boldsymbol{V}_{n+1}, \dot{\boldsymbol{V}}_{n+1}$ and $\ddot{\boldsymbol{V}}_{n+1}$. The parameters $\alpha_f$, $\alpha_m$, $\gamma$ and $\beta$ are chosen as in [4] to ensure second-order accuracy and unconditional stability of the time-integration algorithm.

The non-linear system of equations (38) may be solved using a Newton–Raphson iteration procedure, which leads to the following two-stage predictor-multicorrector algorithm.

**Predictor stage**: There are different options for the predictor phase. Here, a constant-velocity predictor is adopted. Thus, we take

$$\dot{\boldsymbol{U}}_{n+1}^{(0)} = \dot{\boldsymbol{U}}_n,$$
$$\ddot{\boldsymbol{U}}_{n+1}^{(0)} = \frac{\gamma-1}{\gamma}\ddot{\boldsymbol{U}}_n,$$
$$\boldsymbol{U}_{n+1}^{(0)} = \boldsymbol{U}_n + \Delta t\dot{\boldsymbol{U}}_n + \frac{\Delta t^2}{2}\left((1-2\beta)\ddot{\boldsymbol{U}}_n + 2\beta\ddot{\boldsymbol{U}}_{n+1}^{(0)}\right),$$
$$\dot{\boldsymbol{V}}_{n+1}^{(0)} = \dot{\boldsymbol{V}}_n,$$
$$\ddot{\boldsymbol{V}}_{n+1}^{(0)} = \frac{\gamma-1}{\gamma}\ddot{\boldsymbol{V}}_n,$$
$$\boldsymbol{V}_{n+1}^{(0)} = \boldsymbol{V}_n + \Delta t\dot{\boldsymbol{V}}_n + \frac{\Delta t^2}{2}\left((1-2\beta)\ddot{\boldsymbol{V}}_n + 2\beta\ddot{\boldsymbol{V}}_{n+1}^{(0)}\right), \tag{41}$$

where in the above equations, and in what follows, an index with parentheses is the nonlinear iteration index.

**Multicorrector stage**: Repeat the following steps for $i = 1, 2, ..., i_{max}$ or until convergence

1. Evaluate solution iterates at the $\alpha$-levels

$$\boldsymbol{U}_{n+\alpha_f}^{(i)} = \boldsymbol{U}_n + \alpha_f \left( \boldsymbol{U}_{n+1}^{(i-1)} - \boldsymbol{U}_n \right), \tag{42a}$$

$$\dot{\boldsymbol{U}}_{n+\alpha_f}^{(i)} = \dot{\boldsymbol{U}}_n + \alpha_f \left( \dot{\boldsymbol{U}}_{n+1}^{(i-1)} - \dot{\boldsymbol{U}}_n \right), \tag{42b}$$

$$\ddot{\boldsymbol{U}}_{n+\alpha_m}^{(i)} = \ddot{\boldsymbol{U}}_n + \alpha_m \left( \ddot{\boldsymbol{U}}_{n+1}^{(i-1)} - \ddot{\boldsymbol{U}}_n \right), \tag{42c}$$

$$\boldsymbol{V}_{n+\alpha_f}^{(i)} = \boldsymbol{V}_n + \alpha_f \left( \boldsymbol{V}_{n+1}^{(i-1)} - \boldsymbol{V}_n \right), \tag{42d}$$

$$\dot{\boldsymbol{V}}_{n+\alpha_f}^{(i)} = \dot{\boldsymbol{V}}_n + \alpha_f \left( \dot{\boldsymbol{V}}_{n+1}^{(i-1)} - \dot{\boldsymbol{V}}_n \right), \tag{42e}$$

$$\ddot{\boldsymbol{V}}_{n+\alpha_m}^{(i)} = \ddot{\boldsymbol{V}}_n + \alpha_m \left( \ddot{\boldsymbol{V}}_{n+1}^{(i-1)} - \ddot{\boldsymbol{V}}_n \right). \tag{42f}$$

2. Use the solutions at the $\alpha$-levels to assemble the residual and the tangent matrix of the linear system

$$\frac{\partial \boldsymbol{R}_{(i)}^{cont}}{\partial \ddot{\boldsymbol{U}}_{n+1}} \Delta \ddot{\boldsymbol{U}}_{n+1}^{(i)} + \frac{\partial \boldsymbol{R}_{(i)}^{cont}}{\partial \ddot{\boldsymbol{V}}_{n+1}} \Delta \ddot{\boldsymbol{V}}_{n+1}^{(i)} = -\boldsymbol{R}_{(i)}^{cont}, \tag{43a}$$

$$\frac{\partial \boldsymbol{R}_{(i)}^{mom}}{\partial \ddot{\boldsymbol{U}}_{n+1}} \Delta \ddot{\boldsymbol{U}}_{n+1}^{(i)} + \frac{\partial \boldsymbol{R}_{(i)}^{mom}}{\partial \ddot{\boldsymbol{V}}_{n+1}} \Delta \ddot{\boldsymbol{V}}_{n+1}^{(i)} = -\boldsymbol{R}_{(i)}^{mom}, \tag{43b}$$

$$\frac{\partial \boldsymbol{R}_{(i)}^{aux}}{\partial \ddot{\boldsymbol{U}}_{n+1}} \Delta \ddot{\boldsymbol{U}}_{n+1}^{(i)} + \frac{\partial \boldsymbol{R}_{(i)}^{aux}}{\partial \ddot{\boldsymbol{V}}_{n+1}} \Delta \ddot{\boldsymbol{V}}_{n+1}^{(i)} = -\boldsymbol{R}_{(i)}^{aux}, \tag{43c}$$

$$\frac{\partial \boldsymbol{R}_{(i)}^{ener}}{\partial \ddot{\boldsymbol{U}}_{n+1}} \Delta \ddot{\boldsymbol{U}}_{n+1}^{(i)} + \frac{\partial \boldsymbol{R}_{(i)}^{ener}}{\partial \ddot{\boldsymbol{V}}_{n+1}} \Delta \ddot{\boldsymbol{V}}_{n+1}^{(i)} = -\boldsymbol{R}_{(i)}^{ener}, \tag{43d}$$

$$\frac{\partial \boldsymbol{R}_{(i)}^{mesh}}{\partial \ddot{\boldsymbol{U}}_{n+1}} \Delta \ddot{\boldsymbol{U}}_{n+1}^{(i)} + \frac{\partial \boldsymbol{R}_{(i)}^{mesh}}{\partial \ddot{\boldsymbol{V}}_{n+1}} \Delta \ddot{\boldsymbol{V}}_{n+1}^{(i)} = -\boldsymbol{R}_{(i)}^{mesh}. \tag{43e}$$

The resulting linear system is solved using a preconditioned GMRES algorithm.

3. Use $\Delta \ddot{\boldsymbol{U}}_{n+1}^{(i)}$ and $\Delta \ddot{\boldsymbol{V}}_{n+1}^{(i)}$ to update the iterates as

$$\ddot{\boldsymbol{U}}_{n+1}^{(i)} = \ddot{\boldsymbol{U}}_{n+1}^{(i-1)} + \Delta \ddot{\boldsymbol{U}}_{n+1}^{(i)}, \tag{44a}$$

$$\dot{\boldsymbol{U}}_{n+1}^{(i)} = \dot{\boldsymbol{U}}_{n+1}^{(i-1)} + \gamma \Delta t \Delta \ddot{\boldsymbol{U}}_{n+1}^{(i)}, \tag{44b}$$

$$\boldsymbol{U}_{n+1}^{(i)} = \boldsymbol{U}_{n+1}^{(i-1)} + \beta \Delta t^2 \Delta \ddot{\boldsymbol{U}}_{n+1}^{(i)}, \tag{44c}$$

$$\ddot{\boldsymbol{V}}_{n+1}^{(i)} = \ddot{\boldsymbol{V}}_{n+1}^{(i-1)} + \Delta \ddot{\boldsymbol{V}}_{n+1}^{(i)}, \tag{44d}$$

$$\dot{\boldsymbol{V}}_{n+1}^{(i)} = \dot{\boldsymbol{V}}_{n+1}^{(i-1)} + \gamma \Delta t \Delta \ddot{\boldsymbol{V}}_{n+1}^{(i)}, \tag{44e}$$

$$\boldsymbol{V}_{n+1}^{(i)} = \boldsymbol{V}_{n+1}^{(i-1)} + \beta \Delta t^2 \Delta \ddot{\boldsymbol{V}}_{n+1}^{(i)}. \tag{44f}$$

This completes one nonlinear iteration. The nonlinear iterative algorithm should be repeated until the norm of each of the residual vectors defined in (36) has been reduced to a given tolerance $\varepsilon$ of its value using the predictions defined in (41). In this work, we use $\varepsilon = 10^{-4}$.

**Remark** To solve the FSI equations, we adopt a quasi-direct solution strategy (see [76–78] for the definition of terminology and methods), where the fluid and solid equations are solved in a coupled fashion, while the mesh motion equations are solved separately, using the data from the fluid–solid solve as input. As a result, the so-called shape derivatives, that is, the derivatives of the continuity, momentum

and energy residuals with respect to the mesh motion variables, are omitted. It was shown in [4, 19] that omitting shape derivatives has little effect on the convergence of Newton–Raphson iterations, and leads to non-negligible computational savings. In the implementation of the quasi-direct solution strategy, Eqns. (43) in the above predictor-multicorrector algorithm are simplified to

$$\frac{\partial \boldsymbol{R}_{(i)}^{cont}}{\partial \ddot{\boldsymbol{U}}_{n+1}} \Delta \ddot{\boldsymbol{U}}_{n+1}^{(i)} = -\boldsymbol{R}_{(i)}^{cont}, \tag{45a}$$

$$\frac{\partial \boldsymbol{R}_{(i)}^{mom}}{\partial \ddot{\boldsymbol{U}}_{n+1}} \Delta \ddot{\boldsymbol{U}}_{n+1}^{(i)} = -\boldsymbol{R}_{(i)}^{mom}, \tag{45b}$$

$$\frac{\partial \boldsymbol{R}_{(i)}^{aux}}{\partial \ddot{\boldsymbol{U}}_{n+1}} \Delta \ddot{\boldsymbol{U}}_{n+1}^{(i)} = -\boldsymbol{R}_{(i)}^{aux}, \tag{45c}$$

$$\frac{\partial \boldsymbol{R}_{(i)}^{ener}}{\partial \ddot{\boldsymbol{U}}_{n+1}} \Delta \ddot{\boldsymbol{U}}_{n+1}^{(i)} = -\boldsymbol{R}_{(i)}^{ener}, \tag{45d}$$

$$\frac{\partial \boldsymbol{R}_{(i)}^{mesh}}{\partial \ddot{\boldsymbol{V}}_{n+1}} \Delta \ddot{\boldsymbol{V}}_{n+1}^{(i)} = -\boldsymbol{R}_{(i)}^{mesh}, \tag{45e}$$

where the last equation, which governs the deformation of the fluid mechanics mesh, is solved using the solution of the first four equations as input.

# 4 Numerical examples

We present two numerical examples of phase-change-driven implosion of relatively thin structures initially filled with water vapor. The first one corresponds to a cylinder of infinite length, which is modeled as a two-dimensional system. The second one studies the implosive collapse of a three-dimensional box. All the parameters and the results presented in Sect. 4 are given in non-dimensional form. To do so, we have rescaled the units of measurement of length, mass, time and temperature by $L_0$, $bL_0^3$, $L_0/\sqrt{ab}$ and $\theta_c$, respectively, where $L_0 = 1$ denotes a length scale of the computational domain size. Using this non-dimensionalization, it may be shown that the fluid mechanics problem has four dimensionless numbers,

$$Re = \frac{L_0 b \sqrt{ab}}{\bar{\mu}}, \quad Ca = \frac{\sqrt{\lambda/a}}{L_0}, \tag{46}$$

$$Pr = \frac{L_0 a b^2 \sqrt{ab}/\theta_c}{k}, \quad c = \frac{8}{27} \frac{c_v}{R}, \tag{47}$$

where $Re$ is the Reynolds number, $Ca$ denotes the capillary number, $Pr$ is the Prandtl number, and $c$ is the dimensionless heat capacity. The solid mechanics problem has two dimensionless numbers,

$$\hat{\mu} = \frac{\mu}{\rho_0^s ab}, \quad \hat{\kappa} = \frac{\kappa}{\rho_0^s ab}. \tag{48}$$

The capillary number $Ca$ and the Reynolds number $Re$ were chosen according to the methodology proposed in [33], which

is an upscaling method to desensitize the solution to mesh refinement. In particular, we take

$$Ca = h/L_0 \quad \text{and} \quad Re = \alpha L_0/h, \tag{49}$$

where $h$ is a characteristic length scale of the spatial mesh (see [33]) and $\alpha$ is an $O(1)$ constant. Following [33], we have adopted $\alpha = 2$ for all the computations.

**Remark** We note that solving very strong implosions at full scale is extremely difficult from the modeling and computational point of view. First, from the computational point of view, the fluid subdomain volume would be reduced quite dramatically and remeshing would be necessary. Second, very strong implosions are associated to strong temperature reductions in the structure, and the van der Waals equation is significantly less accurate for low temperatures than for high temperatures. For these reasons, we focus on moderately strong implosions.

### 4.1 2D example

Here, we simulate the collapse of a solid ring which is initially filled with water vapor in equilibrium. The external radius of the ring is $L_0 = 1$, and the thickness of the solid is $L_0/40$. We suppose that there is a follower load acting on the solid external surface, which is identical to the water vapor pressure inside the ring, so the system is initially in thermal and mechanical equilibrium. We trigger the implosion by suddenly reducing the temperature at the fluid–solid interface using the temperature boundary condition. The temperature reduction makes the vapor condensate, reducing the internal pressure and increasing the density. Our problem setup is completely symmetric, so we perform the computation on one quarter of the physical domain (see Fig. 3, where we specify the geometry and the boundary conditions of the problem).

Fig. 4 shows the time evolution of the density (left) and temperature (right) in the fluid subdomain. The solid is analyzed only by plotting its deformed configuration (we have also made use of the symmetry for visualization purposes, and we only represent one quarter of the domain). In the NSK theory, the density is a marker of the phases, and in our density color scale, red represents vapor and blue represents liquid. It may be observed that at the initial time, all the fluid subdomain is in gaseous state [Fig. 4(a)]. The thin grey subdomain that encloses the fluid represents the structure. The problem is initialized by taking as initial density, velocity and temperature the values $\rho_0 = 0.1$, $\boldsymbol{v}_0 = 0$ and $\theta_0 = 0.85$, respectively. On the fluid-structure interface we apply a temperature boundary condition given by $\theta_D = 0.5 < \theta_0$ which triggers the implosion. In particular, the temperature of the gas close to the structure is reduced and the gas turns
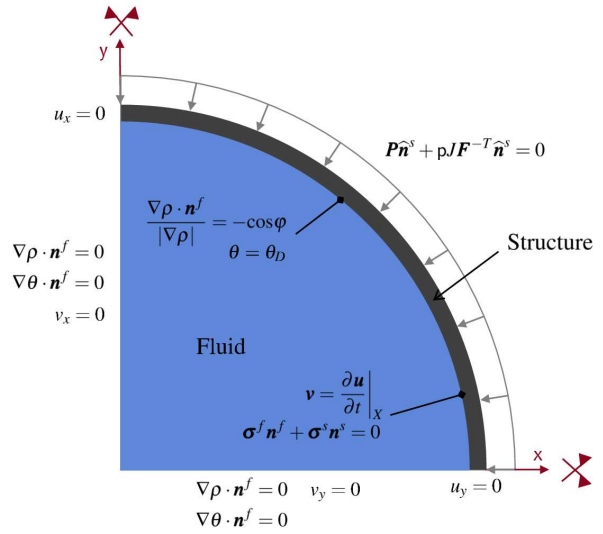


**Fig. 3** Computational domain of the 2D example. The symmetry conditions for the fluid velocity $\boldsymbol{v}$, density $\rho$ and temperature $\theta$, and for the solid displacements $\boldsymbol{u}$ are indicated on the left and bottom boundaries (in the plot, $\square_x$ and $\square_y$ denote the first and second components of the vector $\square$, respectively). The external pressure $\mathsf{p}$ (follower load) acting on the structure and the temperature $\theta_D$ applied at the fluid-structure interface are also depicted. Finally, a certain angle $\varphi$ is imposed between the solid wall and the liquid-vapor interface.

into liquid (blue) [Fig. 4(c)]. The pressure decreases inside and the structure is deformed due to the external pressure [Fig. 4(c)]. The process continues so that all the gas is transformed into liquid and the structure is completely collapsed (data not shown). The parameters employed in this example are $c = 0.73$, $Pr = 0.013$, $Re = 256$, $Ca = 0.0078125$ for the fluid and $\widehat{\mu} = 1.0$ and $\widehat{\kappa} = 1.0$ for the solid. The contact angle was assumed $\varphi = \pi/2$. We used a computational mesh composed of $128^2$ NURBS quadratic elements. The basis functions have a $\mathscr{C}^0$ line on the fluid–structure interface, but otherwise are globally $\mathscr{C}^1$-continuous.

### 4.2 3D example

The setup of this example is identical to that of the two-dimensional problem, but here we focus on the collapse of a three-dimensional box of side $2L_0$. Due to the symmetry our computational domain is a box of side $L_0$, representing one eight of the physical domain. The box is hollow and its thickness is $L_0/40$ [see Fig. 5(a)]. All the parameters and initial conditions are also the same as in Sect. 4.1, but the collapse is stronger because the structure is geometrically softer. Fig. 5 shows the evolution of the density (left) and temperature (right). It is observed that the temperature boundary condition triggers the transformation of vapor into liquid creating a blue area in the density plot which represents liquid water. We used a computational mesh composed of $128^3$ NURBS quadratic elements. The basis func-

(a) $t = 0$                    (b) $t = 0$



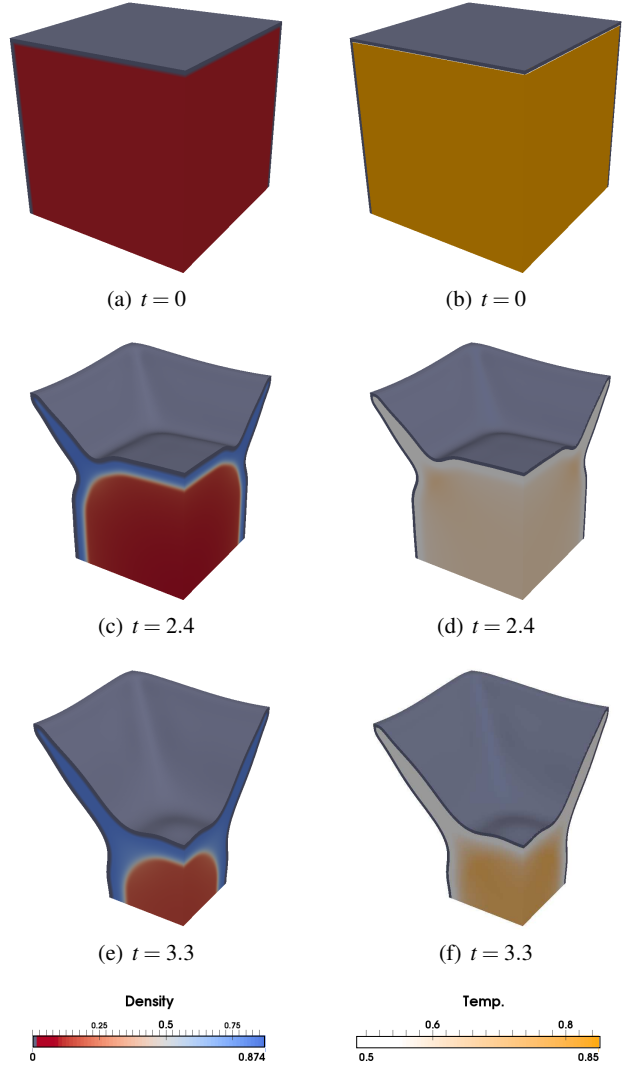(c) $t = 2.8$                    (d) $t = 2.8$
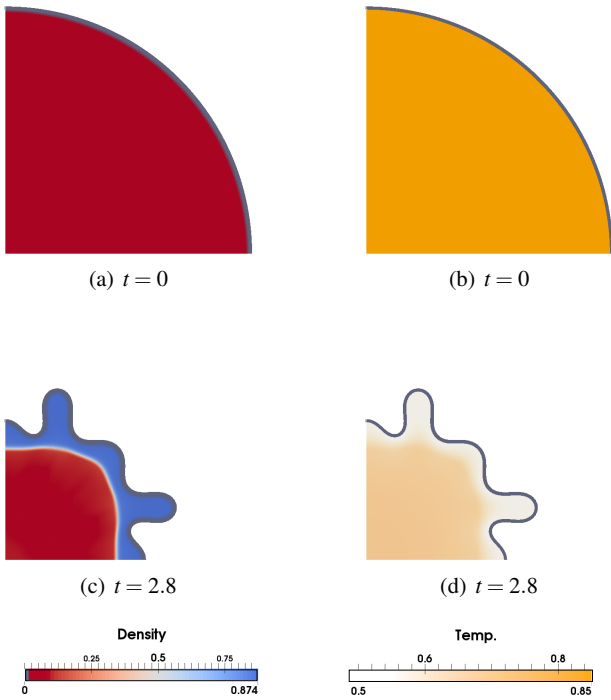
**Fig. 4** Evolution of density (left) and temperature (right) in a 2D phase-change-driven implosion problem. Initially, water-vapor (red color in the density plot) is filling up a hollow structure (a) and a low temperature $\theta_D = 0.5$ is applied at the fluid-structure interface. The vapor close to the boundaries increases its density and turns into liquid [blue in the density plot, (c)]. The pressure inside is reduced and the structure deforms due to the external load. We have used the parameters $Re = 256$, $Ca = 0.0078125$, $Pr = 0.013$, $c = 0.73$, $\hat{\mu} = 1.0$, $\hat{\kappa} = 1.0$.

tions have $\mathscr{C}^0$ lines on the fluid-structure interface, but otherwise are globally $\mathscr{C}^1$-continuous. The time step was selected adaptively using the algorithm proposed in [30].

## 5 Conclusions

We reported on our initial efforts to study computationally the interaction of complex fluids and solids. From a methodological point of view, our theoretical framework and algorithms may be thought of as an extension of well-established FSI methods to the realm of complex fluids. We showed the viability of the approach by way of two numerical examples. Although our examples focus only on phase-change-driven implosion, we believe that our theories and algorithms may be used to solve other, largely unexplored problems that involve the interaction of complex fluids and solids.

(a) $t = 0$                    (b) $t = 0$



(c) $t = 2.4$                    (d) $t = 2.4$



(e) $t = 3.3$                    (f) $t = 3.3$

**Fig. 5** Evolution of density (left) and temperature (right) in a 3D phase-change-driven implosion problem. Initially, water-vapor (red color in the density plot) is filling up a hollow structure (a) and a low temperature $\theta_D = 0.5$ is applied at the fluid-structure interface. The vapor close to the boundaries increases its density and turns into liquid (blue color in the density plot) [(c) and (e)]. The pressure inside is reduced and the structure deforms due to the external load. We have used the parameters $Re = 256$, $Ca = 0.0078125$, $Pr = 0.013$, $c = 0.73$, $\hat{\mu} = 1.0$, $\hat{\kappa} = 1.0$.

## References

1. Y. Bazilevs, L. Beiro Da Veiga, J.A. Cottrell, T.J.R. Hughes, and G. Sangalli. Isogeometric Analysis: Approximation, stability and error estimates for h-refined meshes. *Math. Models Methods Appl. Sci.*, 16(07):1031–1090, 2006.
2. Y. Bazilevs, V.M. Calo, J.A. Cottrell, J.A. Evans, T.J.R. Hughes, S. Lipton, M.A. Scott, and T.W. Sederberg. Isogeometric Analysis using T-splines. *Comput. Methods Appl. Mech. and Eng.*, 199(58):229 – 263, 2010.
3. Y. Bazilevs, V.M. Calo, J.A. Cottrell, T.J.R. Hughes, A. Reali, and G. Scovazzi. Variational multiscale residual-based turbulence modeling for large eddy simulation of incompressible flows. *Comput. Methods Appl. Mech. and Eng.*, 197(14):173 – 201, 2007.

4. Y. Bazilevs, V.M. Calo, T.J.R. Hughes, and Y. Zhang. Isogeometric Fluid-Structure Interaction: Theory, algorithms, and computations. *Comput. Mech.*, 43(1):3–37, 2008.

5. Y. Bazilevs, V.M. Calo, Y. Zhang, and T.J.R. Hughes. Isogeometric Fluid-Structure Interaction analysis with applications to arterial blood flow. *Comput. Mech.*, 38(4-5):310–322, 2006.

6. Y. Bazilevs, J.R. Gohean, T.J.R. Hughes, R.D. Moser, and Y. Zhang. Patient-specific isogeometric fluid–structure interaction analysis of thoracic aortic blood flow due to implantation of the jarvik 2000 left ventricular assist device. *Comput. Methods Appl. Mech. and Eng.*, 198(45):3534–3550, 2009.

7. Y. Bazilevs, M.-C. Hsu, J. Kiendl, R. Wüchner, and K.-U. Bletzinger. 3D simulation of wind turbine rotors at full scale. part II: Fluid–structure interaction modeling with composite blades. *Int. J. Numer. Methods Fluids*, 65(1-3):236–253, 2011.

8. Y. Bazilevs, K. Takizawa, and T. E. Tezduyar. Challenges and directions in computational fluid-structure interaction. *Math. Models Methods Appl. Sci.*, 23:215–221, 2013.

9. Y. Bazilevs, K. Takizawa, and T.E. Tezduyar. *Computational Fluid-Structure Interaction. Methods and applications*. Wiley, 2013.

10. Y. Bazilevs, K. Takizawa, T.E. Tezduyar, M.-C. Hsu, N. Kostov, and S. McIntyre. Aerodynamic and FSI Analysis of Wind Turbines with the ALE-VMS and ST-VMS Methods. *Arch. Computat. Methods Eng.*, published online, DOI: 10.1007/s11831-014-9119-7, May 2014.

11. D.J. Benson, Y. Bazilevs, M.C. Hsu, and T.J.R. Hughes. Isogeometric shell analysis: the reissner–mindlin shell. *Comput. Methods Appl. Mech. and Eng.*, 199(5):276–289, 2010.

12. M.J. Borden, C.V. Verhoosel, M.A. Scott, T.J.R. Hughes, and C.M. Landis. A phase-field description of dynamic brittle fracture. *Comput. Methods Appl. Mech. and Eng.*, 217220(0):77 – 95, 2012.

13. L.-Q. Chen. Phase-field models for microstructure evolution. *Annu. Rev. Mater. Res.*, 32(1):113–140, 2002.

14. J. Chung and G.M. Hulbert. A time integration algorithm for structural dynamics with improved numerical dissipation: The generalized-$\alpha$ method. *J. Appl. Mech.*, 60:371–375, 1993.

15. J.A. Cottrell, T.J.R. Hughes, and Y. Bazilevs. *Isogeometric Analysis: Toward Integration of CAD and FEA*. Wiley, 2009.

16. J.A. Cottrell, T.J.R. Hughes, and A. Reali. Studies of refinement and continuity in Isogeometric structural analysis. *Comput. Methods Appl. Mech. and Eng.*, 196(4144):4160 – 4183, 2007.

17. J.A. Cottrell, A. Reali, Y. Bazilevs, and T.J.R. Hughes. Isogeometric Analysis of structural vibrations. *Comput. Methods Appl. Mech. and Eng.*, 195(4143):5257 – 5296, 2006.

18. L. Cueto-Felgueroso and R. Juanes. Nonlocal interface dynamics and pattern formation in gravity-driven unsaturated flow through porous media. *Phys. Rev. Lett.*, 101:244504, Dec 2008.

19. W.G. Dettmer and D. Peric. On the coupling between fluid flow and mesh motion in the modelling of fluid–structure interaction. *Comput. Mech.*, 43:81–90, 2008.

20. D. Diehl. *Higher order schemes for simulation of compressible liquid-vapor flows with phase change*. PhD thesis, Albert-Ludwigs-Universitat, 2007.

21. J. Donea and A. Huerta. *Finite Element Methods for Flow Problems*. Wiley, 2003.

22. J. Donea, A. Huerta, J.-Ph. Ponthot, and A. Rodrguez-Ferran. *Encyclopedia of Computational Mechanics. Arbitrary Lagrangian-Eulerian Methods.*, volume 1, chapter 14. John Wiley & Sons, Ltd, 2004.

23. J.E. Dunn and J. Serrin. On the thermomechanics of interstitial working. *Arch. Rational Mech. Anal.*, 88(2):95–133, 1985.

24. T. Elguedj, Y. Bazilevs, V.M. Calo, and T.J.R. Hughes. $\bar{B}$ and $\bar{F}$ projection methods for nearly incompressible linear and nonlinear elasticity and plasticity using higher-order NURBS elements. *Comput. Methods Appl. Mech. and Eng.*, 197(3340):2732 – 2762, 2008.

25. C. Farhat, A. Rallu, and S. Shankaran. A higher-order generalized Ghost Fluid Method for the Poor for the three-dimensional two-phase flow computation of underwater implosions. *J. Comput. Phys*, 227(16):7674 – 7700, 2008.

26. C. Farhat, A. Rallu, K. Wang, and T. Belytschko. Robust and provably second-order explicit-explicit and implicit-explicit staggered time-integrators for highly non-linear compressible Fluid-Structure Interaction problems. *Int. J. Numer. Methods Eng.*, 84(1):73–107, 2010.

27. P.K. Galenko, H. Gomez, N.V. Kropotin, and K.R. Elder. Unconditionally stable method and numerical solution of the hyperbolic phase-field crystal equation. *Phys. Rev. E*, 88(1):013310, 2013.

28. W.M. Gelbart and A. Ben-Shaul. The new science of complex fluids. *The Journal of Physical Chemistry*, 100(31):13169–13189, 1996.

29. J.W. Gibbs. *On the Equilibrium of Heterogeneous Substances*. 1874.

30. H. Gomez, V.M. Calo, Y. Bazilevs, and T.J.R. Hughes. Isogeometric Analysis of the Cahn-Hilliard phase-field model. *Comput. Methods Appl. Mech. and Eng.*, 197:43334352, 2008.

31. H. Gomez, L. Cueto-Felgueroso, and R. Juanes. Three-dimensional simulation of unstable gravity-driven infiltration of water into a porous medium. *J. Comput. Phys*, 238:217–239, 2013.

32. H. Gomez and T.J.R. Hughes. Provably unconditionally stable, second-order time-accurate, mixed variational methods for phase-field models. *J. Comput. Phys*, 230(13):5310–5327, 2011.

33. H. Gomez, T.J.R. Hughes, X. Nogueira, and V.M. Calo. Isogeometric Analysis of the isothermal Navier-Stokes-Korteweg equations. *Comput. Methods Appl. Mech. and Eng.*, 199(25-28):1828–1840, 2010.

34. H. Gomez, A. Reali, and G. Sangalli. Accurate, efficient, and (iso) geometrically flexible collocation methods for phase-field models. *J. Comput. Phys*, 262:153–171, 2014.

35. T.J.R. Hughes, J.A. Cottrell, and Y. Bazilevs. Isogeometric Analysis: CAD, Finite Elements, NURBS, exact geometry and mesh refinement. *Comput. Methods Appl. Mech. and Eng.*, 194(3941):4135 – 4195, 2005.

36. T.J.R. Hughes, W.K. Liu, and T.K. Zimmermann. Lagrangian-Eulerian Finite Element formulation for incompressible viscous flows. *Comput. Methods Appl. Mech. and Eng.*, 29(3):329 – 349, 1981.

37. C.M. Ikeda. *Fluid-Structure Interactions. Implosions of shell structures and wave impact on a flat plate*. PhD thesis, University of Maryland, 2012.

38. K.E. Jansen, C.H. Whiting, and G.M. Hulbert. A generalized-$\alpha$ method for integrating the filtered Navier-Stokes equations with a stabilized Finite Element Method. *Comput. Methods Appl. Mech. and Eng.*, 190(34):305 – 319, 2000.

39. A.A. Johnson and T.E. Tezduyar. Mesh update strategies in parallel finite element computations of flow problems with moving boundaries and interfaces. *Comput. Methods Appl. Mech. and Eng.*, 119:73–94, 1994.

40. K. Kamran, R. Rossi, E. Oñate, and S.R. Idelshon. A compressible lagrangian framework for modeling the fluid–structure interaction in the underwater implosion of an aluminum cylinder. *Math. Models Methods Appl. Sci.*, 23(02):339–367, 2013.

41. K. Kamran, R. Rossi, E. Oñate, and S.R. Idelsohn. A compressible lagrangian framework for the simulation of the underwater implosion of large air bubbles. *Comput. Methods Appl. Mech. and Eng.*, 255:210–225, 2013.

42. S. Lipton, J.A. Evans, Y. Bazilevs, T. Elguedj, and T.J.R. Hughes. Robustness of isogeometric structural discretizations under severe mesh distortion. *Comput. Methods Appl. Mech. and Eng.*, 199(5):357–373, 2010.

43. J. Liu. *Thermodynamically consistent modeling and simulation of multiphase flows*. PhD thesis, The University of Texas at Austin, 2014.

44. J. Liu, H. Gomez, J.A. Evans, T.J.R. Hughes, and C.M. Landis. Functional entropy variables: A new methodology for deriving thermodynamically consistent algorithms for complex fluids, with particular reference to the isothermal Navier-Stokes-Korteweg equations. *J. Comput. Phys*, 248:47–86, 2013.

45. C.C. Long, M. Esmaily-Moghadam, A.L. Marsden, and Y. Bazilevs. Computation of residence time in the simulation of pulsatile ventricular assist devices. *Comput. Mech.*, 54:911–919, 2014.

46. C.C. Long, A.L. Marsden, and Y. Bazilevs. Fluid–structure interaction simulation of pulsatile ventricular assist devices. *Comput. Mech.*, 52:971–981, 2013.

47. C.C. Long, A.L. Marsden, and Y. Bazilevs. Shape optimization of pulsatile ventricular assist devices using FSI to minimize thrombotic risk. *Comput. Mech.*, 54:921–932, 2014.

48. O. Penrose and P.C. Fife. Thermodynamically consistent models of phase-field type for the kinetic of phase transitions. *Phys. D: Nonlinear Phenomena*, 43(1):44 – 62, 1990.

49. A.S.D. Rallu. *A Multiphase Fluid-Structure Computational Framework for Underwater Implosion Problems*. PhD thesis, Standford University, 2009.

50. J. Sedzinski, M. Biro, A. Oswald, J-Y. Tinevez, G. Salbreux, and E. Paluch. Polar actomyosin contractility destabilizes the position of the cytokinetic furrow. *Nature*, 476(7361):462–466, 2011.

51. D. Shao, H. Levine, and W-J. Rappel. Coupling actin flow, adhesion, and morphology in a computational cell motility model. *Proceedings of the National Academy of Sciences*, 109(18):6851–6856, 2012.

52. J.C. Simo and T.J.R. Hughes. *Computational Inelasticity*. Springer-Verlag, New Yoirk, 1998.

53. K. Stein, T. Tezduyar, and R. Benney. Mesh moving techniques for fluid–structure interactions with large displacements. *J. Appl. Mech.*, 70:58–63, 2003.

54. I. Steinbach. Phase-field models in materials science. *Modelling Simul. Mater. Sci. Eng.*, 17(7):073001, 2009.

55. H. Suito, K. Takizawa, V.Q.H. Huynh, D. Sze, and T. Ueda. FSI analysis of the blood flow and geometrical characteristics in the thoracic aorta. *Comput. Mech.*, 54:1035–1045, 2014.

56. K. Takizawa. Computational engineering analysis with the new-generation space–time methods. *Comput. Mech.*, 54:193–211, 2014.

57. K. Takizawa, Y. Bazilevs, and T.E. Tezduyar. Space-Time and ALE-VMS techniques for patient-specific cardiovascular Fluid-Structure Interaction modeling. *Arch. Computat. Methods Eng.*, 19(2):171–225, 2012.

58. K. Takizawa, Y. Bazilevs, T.E. Tezduyar, M.-C. Hsu, O. Oiseth, K.M. Mathisen, N. Kostov, and S. McIntyre. Engineering Analysis and Design with ALE-VMS and Space-Time Methods. *Arch. Computat. Methods Eng.*, published online, DOI: 10.1007/s11831-014-9113-0, May 2014.

59. K. Takizawa, Y. Bazilevs, T.E. Tezduyar, C.C. Long, A.L. Marsden, and K. Schjodt. ST and ALE-VMS methods for patient-specific cardiovascular fluid mechanics modeling. *Math. Models Methods Appl. Sci.*, 24:2437–2486, 2014.

60. K. Takizawa, D. Montes, M. Fritze, S. McIntyre, J. Boben, and T.E. Tezduyar. Methods for FSI modeling of spacecraft parachute dynamics and cover separation. *Math. Models Methods Appl. Sci.*, 23:307–338, 2013.

61. K. Takizawa, D. Montes, S. McIntyre, and T.E. Tezduyar. Space–time VMS methods for modeling of incompressible flows at high Reynolds numbers. *Math. Models Methods Appl. Sci.*, 23:223–248, 2013.

62. K. Takizawa, K. Schjodt, A. Puntel, N. Kostov, and T. E. Tezduyar. Patient-specific computational analysis of the influence of a stent on the unsteady flow in cerebral aneurysms. *Comput. Mech.*, 51:1061–1073, 2013.

63. K. Takizawa, H. Takagi, T. E. Tezduyar, and R. Torii. Estimation of element-based zero-stress state for arterial FSI computations. *Comput. Mech.*, 54:895–910, 2014.

64. K. Takizawa, T. E. Tezduyar, R. Kolesar, C. Boswell, T. Kanai, and K. Montel. Multiscale methods for gore curvature calculations from FSI modeling of spacecraft parachutes. *Comput. Mech.*, published online, DOI: 10.1007/s00466-014-1069-2, September 2014.

65. K. Takizawa and T.E. Tezduyar. Space-time computation techniques with continuous representation in time (ST-C). *Comput. Mech.*, 53(1):91–99, 2014.

66. K. Takizawa, T.E. Tezduyar, J. Boben, N. Kostov, C. Boswell, and A. Buscher. Fluid-structure interaction modeling of clusters of spacecraft parachutes with modified geometric porosity. *Comput. Mech.*, 52(6):1351–1364, 2013.

67. K. Takizawa, T.E. Tezduyar, C. Boswell, R. Kolesar, and K. Montel. FSI modeling of the reefed stages and disreefing of the Orion spacecraft parachutes. *Comput. Mech.*, 54(5):1203–1220, 2014.

68. K. Takizawa, T.E. Tezduyar, A Buscher, and S. Asada. Space–time fluid mechanics computation of heart valve models. *Comput. Mech.*, 54:973–986, 2014.

69. K. Takizawa, T.E. Tezduyar, A. Buscher, and S. Asada. Space-time interface-tracking with topology change (ST-TC). *Comput. Mech.*, 54(4):955–971, 2014.

70. K. Takizawa, T.E. Tezduyar, and N. Kostov. Sequentially-coupled space–time FSI analysis of bio-inspired flapping-wing aerodynamics of an MAV. *Comput. Mech.*, 54:213–233, 2014.

71. K. Takizawa, T.E. Tezduyar, S. McIntyre, N. Kostov, R. Kolesar, and C. Habluetzel. Space-time VMS computation of wind-turbine rotor and tower aerodynamics. *Comput. Mech.*, 53(1):1–15, 2014.

72. K. Takizawa, R. Torii, H. Takagi, T.E. Tezduyar, and X.Y. Xu. Coronary arterial dynamics computation with medical-image-based time-dependent anatomical models and element-based zero-stress state estimates. *Comput. Mech.*, 54:1047–1053, 2014.

73. T.E. Tezduyar. Finite element methods for flow problems with moving boundaries and interfaces. *Arch. Computat. Methods Eng.*, 8:83–130, 2001.

74. T.E. Tezduyar, S. Aliabadi, M. Behr, A. Johnson, and S. Mittal. Parallel finite-element computation of 3D flows. *Computer*, 26(10):27–36, 1993.

75. T.E. Tezduyar, M. Behr, S. Mittal, and A.A. Johnson. Computation of unsteady incompressible flows with the finite element methods–space–time formulations, iterative strategies and massively parallel implementations. In *New Methods in Transient Analysis*, PVP-Vol.246/AMD-Vol.143, pages 7–24, New York, 1992. ASME.

76. T.E. Tezduyar and S. Sathe. Modeling of fluid–structure interactions with the space–time finite elements: Solution techniques. *Int. J. Numer. Methods Fluids*, 54:855–900, 2007.

77. T.E. Tezduyar, S. Sathe, R. Keedy, and K. Stein. Space–time finite element techniques for computation of fluid–structure interactions. *Comput. Methods Appl. Mech. and Eng.*, 195(17-18):2002–2027, 2006.

78. T.E. Tezduyar, S. Sathe, and K. Stein. Solution techniques for the fully-discretized equations in computation of fluid–structure interactions with the space–time formulations. *Comput. Methods Appl. Mech. and Eng.*, 195:5743–5753, 2006.

79. U. Thiele, A.J. Archer, M.J. Robbins, H. Gomez, and E. Knobloch. Localized states in the conserved swift-hohenberg equation with cubic nonlinearity. *Phys. Rev. E*, 87(4):042915, 2013.

80. S.E. Turner. Underwater implosion of glass spheres. *J. Acoust. Soc. Am.*, 121(2):844–852, 2007.

81. J.D. van der Waals. The thermodynamic theory of capillarity under the hypothesis of a continuous variation of density. *J. Stat. Phys.*, 20(2):200–244, 1979.

82. G. Vilanova, I. Colominas, and H. Gomez. Capillary networks in tumor angiogenesis: From discrete endothelial cells to phase-field averaged descriptions via isogeometric analysis. *Int. J. Numer. Meth. Biomed. Eng.*, 29(10):1015–1037, 2013.

83. Y. Zhang, Y. Bazilevs, S. Goswami, C.L. Bajaj, and T.J.R. Hughes. Patient-specific vascular NURBS modeling for Isogeometric Analysis of blood flow. *Comput. Methods Appl. Mech. and Eng.*, 196(2930):2943 – 2959, 2007.